# Design of UWB Antenna for Air-Coupled Impulse Ground-Penetrating Radar

Amr Ahmed, Yu Zhang, Dylan Burns, Dryver Huston, and Tian Xia

***Abstract*—This letter presents a new transverse electromagnetic flared horn antenna for the demanding requirement of an air-coupled impulse ground-penetrating radar. Structure anatomy is performed focusing on achieving good impedance matching throughout the wide frequency band. The design procedure starts with constructing an analytic model to evaluate the preliminary physical dimensions to achieve minimum reflections. Structural fine tunings are then performed for optimization. The antennas are fabricated and tested. Experimental results validate the design effectiveness.**

***Index Terms*—Antennas, ground-penetrating radar (GPR), ultrawide bandwidth.**

## I. Introduction

ULTRAWIDEBAND (UWB) ground-penetrating radar (GPR) techniques are increasingly used in nondestructive testing and through-wall imaging for inspections of subsurface structures and buried objects [1]–[5]. In GPR, the antenna plays a significant role in determining system performance. GPR antenna design is very challenging because it requires exceptional impedance matching across the whole ultrawide frequency band.

In general, several types of antennas [5] are used for UWB GPR systems, such as resistively loaded dipole [6], bow-tie antenna [7], spiral antenna [8], and TEM horn antennas [9]. The resistively loaded dipole is simple and easy to design and has linearly polarized antenna structure. However, it has a major limitation of low gain. Bow-tie and spiral antennas are mainly used in ground-coupled GPRs for their nondispersive characteristics, whereas they typically show a high ringing effect, which distorts the time-domain waveform. Resistive loading is usually used to overcome this drawback, but at the price of significant gain loss. TEM horn antenna, on the other hand, has a clear advantage over planar antennas. A typical TEM horn antenna has narrow beamwidth, which facilitates a higher directivity gain over a wider frequency range. The main design challenge of TEM horn antenna is to achieve a good impedance match in order to minimize internal structure reflections.

In this letter, a new horn antenna is designed with the focus to improve impedance matching spanning the whole ultrawide frequency band. Electromagnetic (EM) simulation and structure optimization are performed to smooth out EM signal propagation. Experimental results show that the antennas can achieve very low ringing effects and good signal fidelity.

Manuscript received June 15, 2015; revised September 30, 2015; accepted November 3, 2015. Date of publication November 25, 2015; date of current version December 24, 2015. This work was supported in part by the U. S. Army Research Laboratory and in part by the U. S. Army Research Office under Contract/Grant W911NF-13-1-0301.

The authors are with the School of Engineering, The University of Vermont, Burlington, VT 05405 USA (e-mail: txia@uvm.edu).

Color versions of one or more of the figures in this paper are available online at http://ieeexplore.ieee.org.

Digital Object Identifier 10.1109/LGRS.2015.2498404

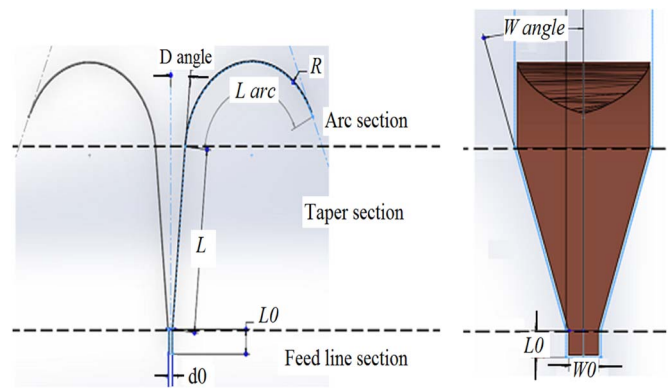


Fig. 1. Top view and side view of the horn antenna.

This letter is organized as follows. Section II presents the anatomy of the proposed horn antenna. Analysis is conducted as the guidelines for structural optimization in Section III. Section IV shows antenna testing results. In Section V, antennas are utilized for impulse GPR tests. The conclusion is given in Section VI.

## II. Antenna Structural Analysis

For impulse GPR antenna design, one challenge is to achieve impedance matching across ultrawide frequency band. There are two main structural points needing intensive considerations: one is the feed port, and the other is the interface at the antenna aperture. For the air-coupled GPR antenna, the characteristic impedance at aperture is 377 Ω, whereas the feed line impedance is 50 Ω. Design measures need to resolve this mismatch by gradually accomplishing impedance transition to minimize reflections.

Fig. 1 illustrates our developed UWB antenna. As shown, the antenna structure consists of three sections: feed line, waveguide taper segment, and a round-shaped aperture. The feed line and the taper section can be modeled as a series of $N$ parallel-plate transmission line segments. Each segment consists of two metal plates that are separated by a dielectric media with varying widths.

Starting with the feed line, the relationship between its input impedance and output impedance is characterized by

$$Z_{\text{in}} = Z_0 \frac{Z_{\text{out}} + jZ_0 \tan(\beta l)}{Z_0 + jZ_{\text{out}} \tan(\beta l)} \tag{1}$$

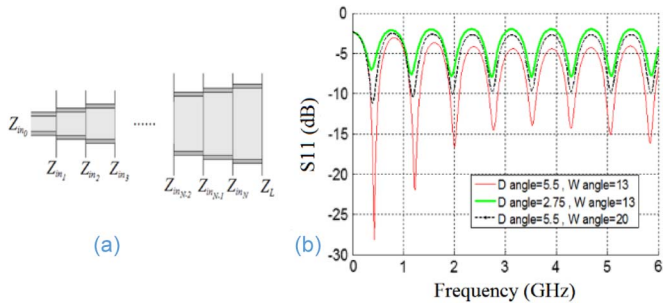


Fig. 2. (a) Taper segment modeling. (b) Simulated S11 for the feed point and the taper segment variables.

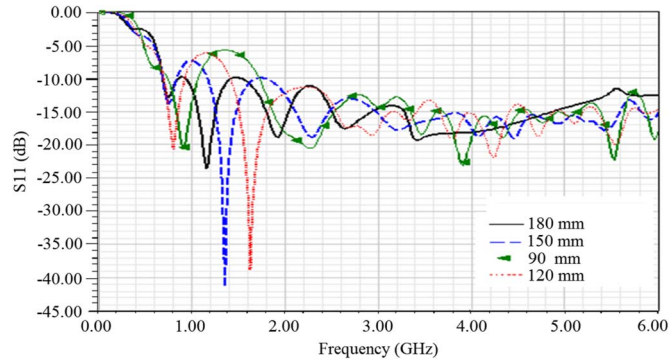


Fig. 3. S11 for different taper lengths.

where $Z_{\text{in}}$ and $Z_{\text{out}}$ are the input and output impedances, respectively; and $l$ is the length of the feed line. $Z_0$ is the characteristic impedance, and $\beta$ is the wavenumber of the transmission line.

In order to characterize the parallel-plate structure, an analytical model is developed to study the effect of feed point length L0 on feed line input impedance across a wide frequency band. The model assumes 50-Ω output impedance, which is replaced by the actual input impedance of the taper section later in the full model. W0 is the feed line width, and d0 is the feed line height. Simulations show that, when $\text{L0} = 6$ mm, $\text{d0} = 3$ mm, and $\text{W0} = 12$ mm, the feed line demonstrates minimal impedance variations across the frequency band ranging from 600 MHz to 6 GHz.

For the waveguide taper section, for simplification, it can be modeled as a staircase structure, as shown in Fig. 2(a), consisting of $N$ segments. Each segment can be assumed homogenous when the segment length is small in comparison with signal wavelength. To minimize the discontinuity effect between the adjacent segments, in the modeling, a large $N$ value is selected for segmenting the taper section and reducing each segment length, which smooths out the structure transition and leverage modeling accuracy.

The input impedance $Z_{\text{in}}$ of each segment can be calculated using

$$Z_{\text{in}_i} = Z_{0_i} \frac{Z_{\text{in}_{i+1}} + jZ_{0_i} \tan(\beta_i l_i)}{Z_{0_i} + jZ_{\text{in}_{i+1}} \tan(\beta_i l_i)} \quad \forall i = 0, \ldots, (N-1) \tag{2}$$

where $\beta_i$, $Z_{0_i}$, and $l_i$ are the wavenumber, the characteristic impedance, and the length of the $i$th segment, respectively. $Z_{\text{in}_{i+1}}$ is the input impedance of the $(i+1)$th stage loading the $i$th segment. The zeroth segment is the touching point between the feed line and the taper section. The $N$th segment is the end of the taper section connecting the aperture arc.

An analytical model is created based on (2) to identify suitable values for $D$_angle and $W$_angle shown in Fig. 1. In the model, the loading impedance of the last stage $Z_L$ is equal to the free-space characteristic impedance (377 Ω). The $N$th segment of the taper section is chosen to interface directly with air, dropping out the arc section for simplicity. For model characterization, parametric analysis is performed, where $D$_angle is swept from 2.75° to 5.5° with a step size of 0.25°, and $W$_angle is swept from 13° to 20° with a step size of 0.5°. Fig. 2 shows S11 results at the start and end points of each sweep range for simplicity. It shows that, when $D$_angle takes the largest value 5.5° and $W$_angle takes the smallest value 13°, minimum S11 results are achieved across the wide frequency range.

## III. Structural Optimization

An antenna 3-D structure model is created using the modeling program SolidWorks, which is then imported into the EM simulation program Ansoft HFSS for EM characterization. HFSS simulation results provide design guides for tuning up structural variables to achieve optimum performance.

One critical design variable is the length of the taper section. Parametric simulations are performed to evaluate the effects of taper section length on S11. Fig. 3 illustrates the simulation results when the length is linearly changed from 90 to 180 mm, with a step size of 30 mm. It is observed that 180-mm length produces steady S11 curve below −10 dB across the whole frequency band.

The shape and length of the arc section also stand as critical design variables. Given that the desired lowest end frequency is 600 MHz, whose full wavelength is 500 mm, the total length of the antenna is chosen to be half of the wavelength. Hence, the arc and the taper section length (= 180 mm) should add up to 250 mm. Simulation result confirms that the initial arc length value of 70 mm is proven to be optimum.

To further improve antenna performance, extra structure optimization measures are taken. As described in [13], for the impulse GPR antenna, its time-domain response signal consists of two regions: one is the transient region resulting from the direct radiation of the excitation pulse, and the other is the undesired resonance region due to the antenna internal structure reflection, which causes sensing signal distortion and needs to be eliminated. In many impulse GPR antenna design practices, resistive loading is applied to absorb the internal structure reflection, however, at the cost of the antenna gain loss. In this design, we take a different approach by reducing the abruptly changing structure. Its fundamental rational is to smooth out EM signal flow so that the internal structure reflection is alleviated.

In the implementation, the optimization is first achieved by rounding the edges at the feed point. Fig. 4(a) and (b) shows the traditional sharp edges versus the edge rounding at feed point, respectively. Results in Fig. 4(c) obviously demonstrate that the rounded-corner structure leads to better S11 performance.

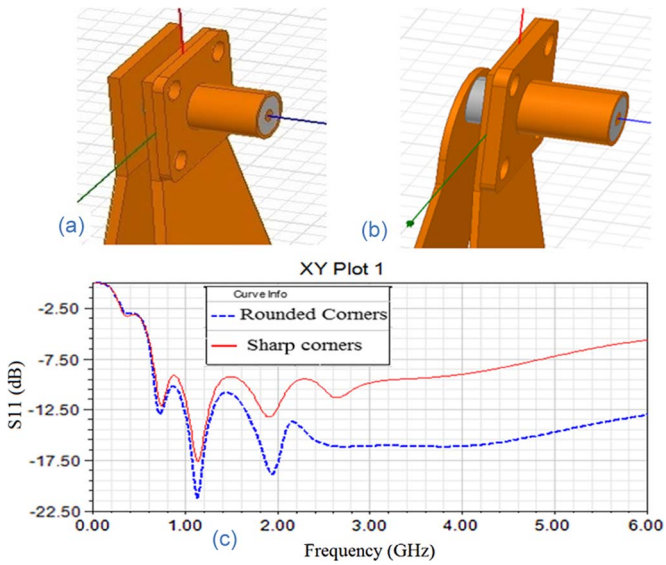


Fig. 4. Feed point (a) sharp corners and (b) rounded corners. (c) S11 simulation results.

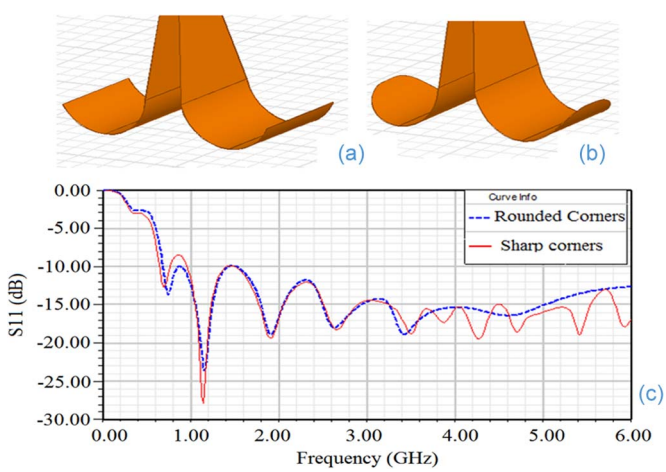


Fig. 5. Flare edges of the antenna. (a) Sharp corners and (b) rounded edges. (c) S11 simulation results.

Rounding the flare edges of the antenna, as illustrated in Fig. 5, also improves the final S11 performance. Fig. 5(c) shows that rounding the sharp corners improves antenna performance at lower frequency end, whereas at upper frequency end, S11 remains below $-10$ dB.

For checking the radiation pattern, a midrange frequency of 2.8 GHz is selected. The corresponding 2-D radiation pattern is plotted in Fig. 6(a), whereas the 3-D polar plot is illustrated in Fig. 6(b). As shown in the figures, the antenna peak gain value at 2.8 GHz is approximately 9.91 dBi. From the 3-D polar plot, it is observed that the radiation power concentrates in the $x-y$ plane, which illustrates its linear polarity.

## IV. Measurement Results

After updating the SolidWorks mechanical model with the optimum design parameters verified by HFSS simulation, prototype antennas are manufactured, as shown in Fig. 7(a).

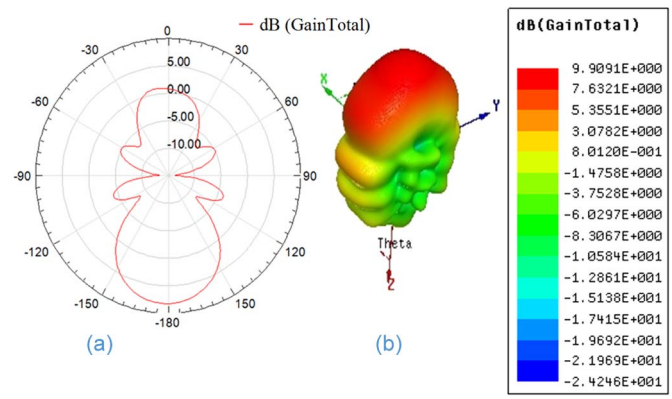


Fig. 6. (a) Radiation pattern. (b) 3-D polar plot (2.8 GHz).

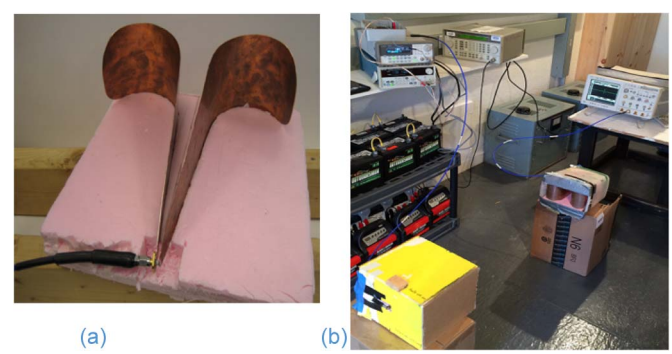


Fig. 7. (a) Fabricated antenna. (b) Direct pulse signals transmission and receiving.

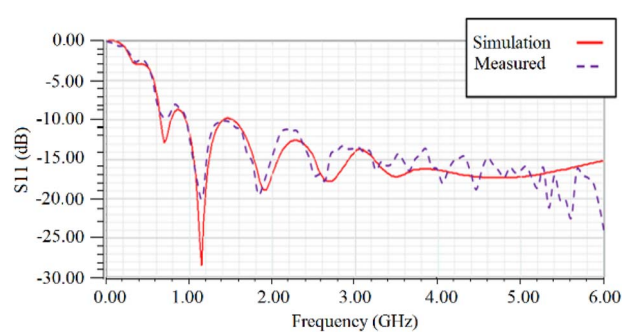


Fig. 8. S11 measurement versus simulation.

S11 measurement is performed using an HP 8753D network analyzer over the frequency band spanning from 100 MHz to 6 GHz with a 20-MHz step. Fig. 8 shows that the measurement results match the simulation results sweeping over the whole spectrum.

The test setup in Fig. 7(b) uses a pair of antennas to transmit and receive time-domain pulse signals generated in our impulse GPR system [11], [12]. The transmitted signal is a Gaussian pulse that has a pulsewidth of approximately 600 ps and an amplitude of approximately 18 V, as shown in Fig. 9 (attenuated by $-20$ dB for measurement). The receiver antenna is placed 1 m away from the transmitter and is connected to the oscilloscope to capture the signal waveform.

The same experiment is repeated using a pair of A.H. Systems double-ridge guide horn antennas SAS-571 [10] for performance comparison. Fig. 10(a) shows that, using our

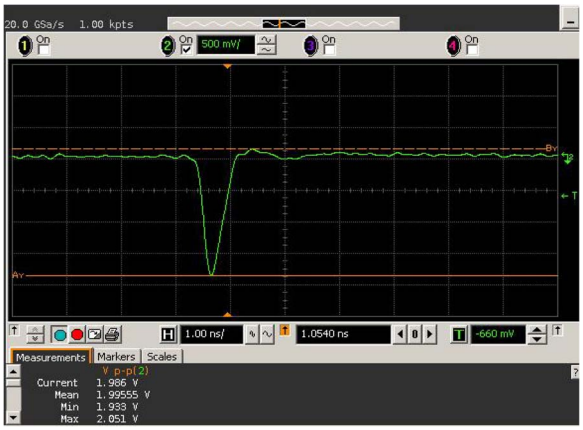


Fig. 9. Pulse signal upon −20-dB attenuation for measurement convenience.

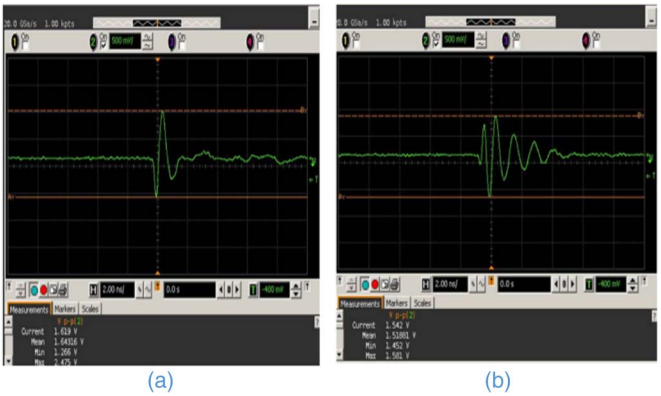


Fig. 10. Received pulse signals (a) with our antennas and (b) with A.H. horn antennas.

developed antennas, the received pulse features smaller ringing effect than using the double-ridge guide horn, whose receiving pulse signal is shown in Fig. 10(b).

For further electrical characterizations, the free-space far-field radiation pattern is measured. The test setup is shown in Fig. 11 using an isotropic antenna as a receiver placed 1 m apart from our transmitter antenna. Note that, as the lower end GPR operating frequency is 600 MHz, whose wavelength is 0.5 m, the 1-m measurement distance meets the far-field criteria. The transmitter antenna is placed on top of a frame on a rotating table that allows measuring radiating peak power over E-plane angles from 0° to 180° with a step size of 10°. The open area test site is equipped with buried grounded mesh acting as a perfect ground plane.

For every single frequency in the sweep, the reading of the received RF voltage $V_{\mathrm{RF}}$ is captured in volts and converted to dBV using

$$V_{\mathrm{RF}}(\mathrm{dBV}) = 20\ \log_{10}\left[V_{\mathrm{RF}}(\mathrm{V})\right]. \tag{3}$$

The losses due to cables and connectors are determined by connecting the cable under test between the signal generator and the spectrum analyzer at the frequency of interest for examination.

The antenna calibration is then performed, which starts with replacing our transmitter antenna with the SAS-571 double-ridge guide horn antenna and measuring the peak power received at the same frequency point. The readings are then compared with the SAS-571 datasheet [10] as the reference for our antenna measurement calibration. Fig. 12 shows the measured radiation patterns and patterns obtained from simulations at the selected frequencies of 2.8 and 1.9 GHz, respectively. Note that the solid line in both figures represents the simulated radiation pattern over E-plane angles from 0° to 360° with a step size of 1°. For our measurements, due to the physical setup constraints, the radiation patterns are only measured within angles from 0° to 180°. As can be observed, the measurement results and the simulation results achieve reasonably good agreements. Moreover, the patterns at both frequencies show a high resemblance.

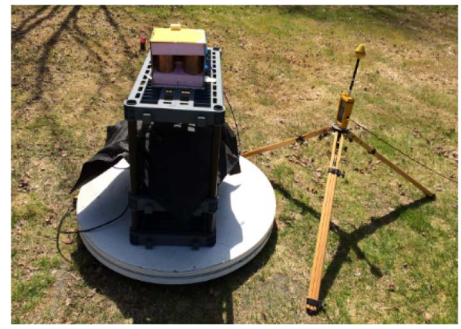

Fig. 11. Radiation measurement setup.

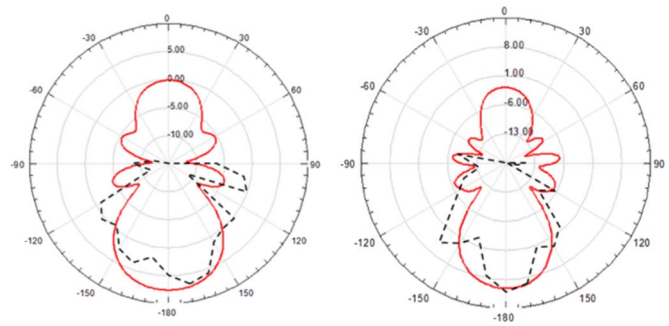


Fig. 12. (Dashed line) Measurement versus (solid line) simulation radiation patterns. (a) 2.8 GHz. (b) 1.9 GHz.

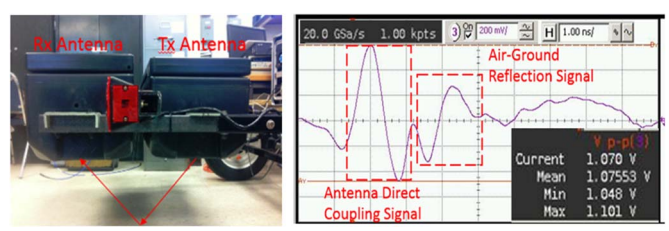


Fig. 13. (a) GPR system. (b) A-scan waveform.

## V. GPR Experiments

To evaluate antenna performance in GPR application, experiments are conducted using our developed GPR system [4], [11], [12]. As shown in Fig. 13(a), the transmitter and receiver antennas are packed in two boxes mounted on a trailer.

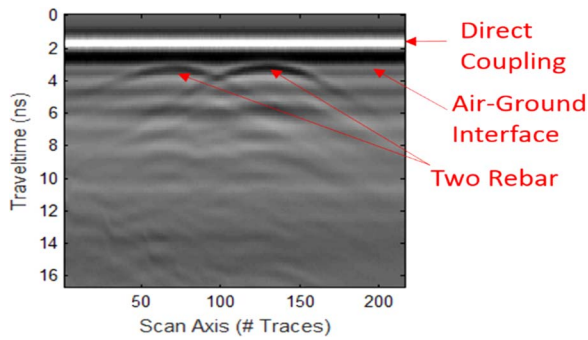


Fig. 14. B-scan image for two rebars on floor test.

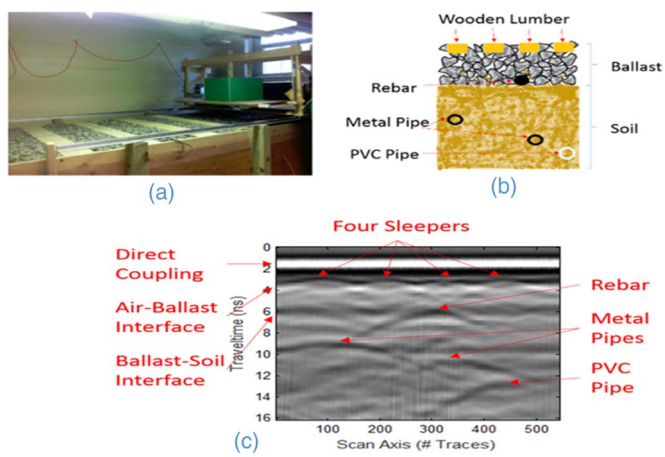


Fig. 15. (a) Test platform emulating a railroad segment. (b) Subsurface structure diagram. (c) B-scan image.

A stationary test is first conducted to measure A-scan waveform collected by the antenna. As shown in Fig. 13(a), the GPR system is stationary, and the antennas are located 14 in above the concrete ground. The A-scan reflection pulse signal recorded is displayed in Fig. 13(b). On the waveform, there are two monocycle pulses featuring the antennas direct coupling signal and the ground surface reflection signal. The pulse shape validates that the antennas can effectively transmit and receive pulse signals with good fidelity. To evaluate antenna operations in a moving GPR, two B-scan tests are also performed. First, two rebars of 1-in diameter each are placed on the ground floor 14 in below scanning antennas. As shown in Fig. 14, two hyperbola signature patterns corresponding to rebars are clearly captured.

For further evaluation, a platform emulating the railroad structure consisting of sleepers, ballast, and buried objects is utilized, as shown in Fig. 15(a). Four sleepers 1 ft apart are placed on top of the ballast layer. Fig. 15(b) illustrates the subsurface structural configuration, which is as follows.

1) The ballast layer is 8 in thick.
2) One rebar of 1-in diameter is buried at the ballast–soil interface.
3) Two metal pipes (diameter: 2 in) and one polyvinyl chloride (PVC) pipe (diameter: 4 in) are buried inside the soil layer. Their burying depths are 18, 24, and 26 in, respectively.

TABLE I
ANTENNA STRUCTURAL SIZE

| | | | |
|---|---|---|---|
| Antenna total length | 250 mm | D_angle | 5.5° |
| Taper segment length | 180 mm | W_angle | 13° |
| Arc section length | 70 mm | Feed point width | 12 mm |
| Feed point length | 6 mm | | |

Fig. 15(c) is the obtained B-scan image, where the subsurface object features, including four hyperbola curves representing timber ties, i.e., one hyperbola for rebar, two hyperbolas for metal pipes, and one hyperbola for PVC pipe, are all clearly observable.

All these experimental results validate the performance of our developed antennas and their suitability in air-coupled impulse GPR application.

## VI. CONCLUSION

This letter has presented from initial concept to manufacturing and final test validation of a new UWB antenna for an air-coupled GPR application. In the design, major structural variables are identified for optimization, whose values are listed in Table I. Experiments prove that antennas can effectively transmit and receive pulse signals with good fidelity.

## REFERENCES

[1] D. J. Daniels, *Ground Penetrating Radar*. Hoboken, NJ, USA: Wiley, 2005.
[2] R. S. Vickers, "Ultra-wideband radar-potential and limitations," in *Proc. IEEE Microw. Symp. Dig.*, 1991, pp. 371–347.
[3] M. Cherniakov and D. Lidia. "Frequency band selection of radars for buried object detection," *IEEE Trans. Geosci. Remote Sens.*, vol. 37, no. 2, pp. 838–845, Mar. 1999.
[4] A. Venkatachalam, X. L. Xu, D. Huston, and T. Xia, "Development of a new high speed dual-channel impulse ground penetrating radar," *IEEE J. Sel. Topics Appl. Earth Observ. Remote Sens.*, vol. 6, no. 3, pp. 753–760, Dec. 2013.
[5] J. R. Andrews, "UWB signal sources, antennas & propagation," in *Proc. IEEE Top. Conf. Wireless Commun. Technol.*, 2003, pp. 439–440.
[6] H. Yang and K. Kangwook, "Ultra-wideband impedance matching technique for resistively loaded Vee dipole antenna," *IEEE Trans. Antennas Propag.*, vol. 61, no. 11, pp. 5788–5792, Nov. 2013.
[7] A. A. Lestari, A. G. Yarovoy, and L. P. Ligthart. "RC-loaded bow-tie antenna for improved pulse radiation," *IEEE Trans. Antennas Propag.*, vol. 52, no. 10, pp. 2555–2563, Oct. 2004.
[8] P. R. Lacko *et al.* "Archimedean-spiral and log-spiral antenna comparison," in *Proc. SPIE Detect. Remediation Technol. Mines Minelike Targets*, 2002, pp. 1–7.
[9] A. S. Turk, A. K. Keskin. "Vivaldi shaped TEM horn fed ridged horn antenna design for UWB GPR systems," in *Proc. IWAGPR*, 2011, pp. 1–4.
[10] Double Ridge Guide Horn Antenna, A. H. Systems, Chatsworth, CA, USA, Jun. 2014.
[11] T. Xia, X. L. Xu, A. Venkatachalam, and D. Huston, "Development of a high speed UWB GPR for rebar detection," in *Proc. Int. Conf. GPR*, 2012, pp. 66–70.
[12] Y. Zhang, P. Candra, G. A. Wang, and T. Xia, "2D entropy and short-time Fourier transform to leverage GPR data analysis efficiency," *IEEE Trans. Instrum. Meas.*, vol. 64, no. 1, pp. 103–111, Jan. 2015.
[13] R. V. D. Jongh, A. G. Yarovoy, L. Lightart, I. Kaploun, and A. Schukin, "Design and analysis of new GPR antenna concepts," in *Proc. Int. Conf. Ground Penetrating Radar*, May 1998, pp. 1–6.
[14] T. Xia, A. Venkatachalam, and D. Huston, "A high-performance low-ringing ultrawideband monocycle pulse generator," *IEEE Trans. Instrum. Meas.*, vol. 61, no. 1, pp. 261–266, Jan. 2012.